RAA 2017 Vol. **17** No. **5**, 47 (16pp) doi: 10.1088/1674–4527/17/5/47

http://www.raa-journal.org *http://iopscience.iop.org/raa*

***R**esearch in*
***A**stronomy and*
***A**strophysics*

Ionized gas clouds near the Sagittarius Arm tangent

Li-Gang Hou[1], Jian Dong[2], Xu-Yang Gao[1] and Jin-Lin Han[1]

[1] National Astronomical Observatories, Chinese Academy of Sciences, Beijing 100012, China; *lghou@nao.cas.cn*
[2] Shanghai Astronomical Observatory, Chinese Academy of Sciences, Shanghai 200030, China

Received 2016 July 26; accepted 2017 February 6

Abstract Radio recombination lines (RRLs) are the best tracers of ionized gas. Simultaneous observations of multi-transitions of RRLs can significantly improve survey sensitivity. We conducted pilot RRL observations near the Sagittarius Arm tangent by using the 65-m Shanghai Tian Ma Radio Telescope (TMRT) equipped with broadband feeds and a digital backend. Six hydrogen RRLs (H96α−H101α) at C band (6289 MHz−7319 MHz) were observed simultaneously toward a sky area of $2^\circ \times 1.2^\circ$ by using on-the-fly mapping mode. These transitions were then stacked together for detection of ionized gas. Star forming complexes G48.6+0.1 and G49.5−0.3 were detected in the integrated intensity map. We found agreements between our measured centroid velocities and previous results for the 21 known HII regions in the mapped area. For more than 80 cataloged HII region candidates without previous RRL measurements, we obtained new RRL spectra at 30 targeted positions. In addition, we detected 25 new discrete RRL sources with spectral S/N $> 5\sigma$, and they were not listed in the catalogs of previously known HII regions. The distances for 44 out of these 55 new RRL sources were estimated.

Key words: Galaxy: disk — radio lines: ISM — ISM: HII regions

1 INTRODUCTION

The interstellar medium (ISM) consists of ionized gas, atomic and molecular clouds, as well as dust, cosmic rays and magnetic fields. Among them, the ionized component generally exists in three forms: individual HII regions, warm ionized gas and hot ionized gas, accounting for ∼20% – 50% of the total gas mass (Lequeux 2005; Ferrière et al. 2007). Radio recombination lines (RRLs) are relatively free of interstellar absorption and extinction. They are the best tracers for ionized gas because of their well-understood physics (Gordon & Sorochenko 2009), the line density of RRL spectra (see Thompson et al. 2015) and their inherent information about dynamics. There has been a wealth of surveys on interstellar atomic gas such as the HI 21cm line (e.g., Kalberla et al. 2005, McClure-Griffiths et al. 2005) and molecular gas by analyzing CO (e.g., Dame et al. 2001, Dempsey et al. 2013; Rigby et al. 2016). But to better understand the global properties of ionized gas in our Galaxy, a great deal of effort in observations at different radio frequencies is necessary (Gordon & Sorochenko 2009; Thompson et al. 2015).

Table 1 shows most surveys were at frequencies below 1.7 GHz, where $T_{\rm line}/T_{\rm continuum}$ is small because the Stark broadening shifts radiation energy from the line core to the line wings and the free-free continuum emission transforms from optically thin to optically thick (Gordon & Sorochenko 2009). Non-local thermodynamic equilibrium (LTE) effects make it not straightforward to get reliable estimates of physical parameters, e.g., electron temperature $T_{\rm e}$ and electron density $n_{\rm e}$. The existing RRL surveys have not covered the entire Galactic plane, especially in the first and second Galactic quadrants. The main limitation of RRL observations is the intrinsic faintness (∼ a few mJy to tens of mJy, Lockman 1989; Anderson et al. 2011) at high quantum number transitions, e.g., quantum number $n > 40$, so that it is very time consuming to conduct a well-sampled and sensitive survey with a single RRL. Many previous papers focused on the discovery of individual bright HII regions by pointing observations of RRLs (e.g., Downes et al. 1980; Caswell & Haynes 1987; Lockman et al. 1996; Anderson et al. 2011; Bania et al. 2012; Du et al. 2011; Han et al. 2011).

Table 1 Previous RRL Surveys toward the Galactic Plane

Reference/Telescope	RRLs	Rest Freq. (MHz)	HPBW	Longitude coverage	Latitude coverage	Sampling
(1)	(2)	(3)	(4)	(5)	(6)	(7)
gc72: Onsala 26-m	H157α	1683.2	$33'$	$9.4^\circ - 130^\circ$	$b = 0^\circ/0.4^\circ$	separation $\delta l > 4^\circ$
hp76: Mark II 38.1-m×25.4-m	H166α	1424.7	$31' \times 33'$	$5^\circ - 70^\circ$	$b = 0^\circ$	separation $\delta l = 0.5^\circ$ /1°/2°
lock76: NRAO 43-m	H166α	1424.7	$21'$	$358^\circ - 0^\circ - 50.5^\circ$	$b = 0^\circ$	separation $\delta l \sim 1^\circ$
cahc89,cahc90: IAR 30-m	H166α	1424.7	$34'$	$298^\circ - 0^\circ - 4^\circ$	$b = 0^\circ$	separation $\delta l = 1^\circ$
hrk96: HCRO 26-m, NRAO 43-m	H165α/167α or H157α/158α or H165α/168α/169α	1350.4−1683.2	$36'/21'$	$357^\circ - 0^\circ - 254.4^\circ$	$\|b\| \geq 0.6^\circ$	583 positions
acwc97: NARO 43-m	H166α	1424.7	$21'$	$60^\circ - 90^\circ$	$b = 0.0^\circ$ /$\pm 0.5^\circ$/ $\pm\ 1.5^\circ$	separation $\delta l = 1^\circ$
				$l = 81^\circ, 83^\circ$	$-4^\circ - +5^\circ$	separation $\delta b = 1^\circ$
ra00, ra01: ORT 530-m×30-m	H270α−273α	321.4 − 332.2	$2^\circ \times 2^\circ$	$332^\circ - 0^\circ - 89^\circ$	$b = 0^\circ$	separation $\delta l > 2^\circ$
				$172^\circ - 252^\circ$	$b = 0^\circ$	14 positions
cmf+09: Parkes 64-m	H166α	1424.7	$16'$	$267^\circ - 302^\circ$	$-3.0^\circ - +1.5^\circ$	Nyquist
lmt+13: Arecibo 300-m, ongoing	H163α−H174α	1237.6 − 1504.6	$3.3' - 3.4'$	$30^\circ - 75^\circ$	$\|b\| \leqslant 2^\circ$	Nyquist
				$175^\circ - 207^\circ$	$-2^\circ - +1^\circ$	
acd+15: Parkes 64-m	H166α−H168α	1374.6 − 1424.7	$14.0' - 14.5'$	$196^\circ - 0^\circ - 52^\circ$	$\|b\| \leqslant 5^\circ$	Nyquist
bbo+15: VLA	19 Hα RRLs	1000 − 2000	$20''^\dagger$	$15^\circ - 67^\circ$	$\|b\| \leqslant 1^\circ$	Nyquist

Notes: Column (1) gives the reference(s) and the telescope(s) used to conduct the survey; Col. (2) lists the observed RRLs and the corresponding line frequencies in MHz are given in Col. (3); Col. (4) is the half power beamwidth (HPBW); Cols. (5) and (6) are the Galactic longitude and latitude coverage of the survey; Col. (7) is a note about the sampling, in which "Nyquist" means that the mapping observations are Nyquist sampled. References: acd+15: Alves et al. (2015); acwc97: Azcárate et al. (1997); cahc89: Cersosimo et al. (1989); cahc90: Cersosimo (1990); cmf+09: Cersosimo et al. (2009); gc72: Gordon & Cato (1972); hp76: Hart & Pedlar (1976); hrk96: Heiles et al. (1996); lmt+13: Liu et al. (2013); lock76: Lockman (1976); ra00: Roshi & Anantharamaiah (2000); ra01: Roshi & Anantharamaiah (2001); bbo+15: Bihr et al. (2015).
Note: "†" indicates that it is a synthesized beam size.

With broadband feeds/receivers and a digital backend, simultaneous observations of multi-transitions of RRLs can be easily stacked to improve the survey sensitivity for ionized gas. The method has been successfully applied in searching for weak individual HII regions (e.g., Anderson et al. 2011; Bania et al. 2012) and blind RRL surveys at frequencies <2 GHz (e.g., Alves et al. 2015). For the RRLs with frequencies above 3 GHz, the observed $T_{\rm line}/T_{\rm continuum}$ is very close to the LTE values (Gordon & Sorochenko 2009), so that it is straightforward to estimate $T_{\rm e}$ and $n_{\rm e}$ together with radio continuum data. At present, well-sampled and sensitive surveys of higher frequency RRLs (>3 GHz) have become feasible and can be complementary to existing multi-wavelength surveys toward our Galaxy (e.g., Kalberla et al. 2005; Dame et al. 2001; Alves et al. 2015). The blind survey data of RRLs would be valuable in detecting new HII regions, mapping the structure of ionized gas clouds in the Milky Way and studying their properties. The newly constructed 65-m Shanghai Tian Ma Radio Telescope (TMRT) was equipped with broadband feeds/receivers and a digital backend, which enables us to conduct an RRL survey toward the northern Galactic plane. Here, we report a pilot observation near the Sagittarius Arm tangent.

2 OBSERVATIONS AND DATA REDUCTION

Observations were conducted from 2015 August 31 to 2015 September 2 by using the TMRT, which is located in the western suburbs of Shanghai. The C band receiver (4.0−8.0 GHz) and mode 2[1] of the digital backend system (DIBAS) were used for observations in a spectral window at a central frequency of 6660 MHz with a bandwidth of 1500 MHz. The number of channels was

[1] *http://radio.shao.cas.cn/para/65mpara/*

set to be 16384, resulting in a spectral resolution of 91.553 kHz.

The observation parameters are summarized in Table 2. The intensity is calibrated by injection of periodic noise with an accuracy of about 20% (Li et al. 2016). The main beam efficiency is 0.6 (Wang et al. 2015; Li et al. 2016). The conversion factor of the main beam temperature into flux density is 0.9 Jy K^{-1}. The targeted area for the pilot survey covers the Galactic longitude range of $48.1^\circ \leqslant l \leqslant 50.1^\circ$ and Galactic latitude range of $-1.0^\circ \leqslant b \leqslant 0.2^\circ$ near the Sagittarius Arm tangent ($l \sim 49.4^\circ$, Hou & Han 2015). We scanned the sky area with the on-the-fly mode along the Galactic longitude and Galactic latitude directions with a speed of $1'\,s^{-1}$. Spectra were recorded every 0.8 s at intervals of $0.8'$. The integration time was about 10 s per pixel to achieve a sensitivity of $T_{\rm MB}$ ∼9 mK (corresponding to a flux density of ∼8 mJy) with a velocity resolution of about 4.4 km s^{-1} for the pilot observation. The off-source points were observed every five scan rows and used to calibrate the on-source observations in each scan row. We checked available data from the 1.4 GHz RRL survey (Alves et al. 2015) and the radio continuum survey (Stil et al. 2006) to ensure no RRLs have been detected in the off-source points. During observations, the continuum emission in the line-free channels were also recorded. However, we found that the continuum map suffered a serious scanning effect, i.e., having many broad and zonal emission features as shown both in the longitude and latitude scanning directions, which may be caused by radio frequency interference and/or gain variations, which cannot be removed with high confidence. The standing wave problem and the separation of non-thermal and thermal continuum emissions (e.g., Xu et al. 2013) make the continuum data reduction more complex. In comparison, the influence of the scanning effect and the standing wave can be easily removed for RRL data by a base-line fitting. In this work, we only focus on RRL data.

The bandpass corrected spectra were processed by using the GILDAS software package[2]. For each of the six observed hydrogen RRLs (see Table 2), we first extracted their spectra in the velocity range ($V_{\rm LSR}$) from -80 km s^{-1} to +150 km s^{-1} (see Fig. 1), and then inspected possible radio frequency interference. The data were gridded using XY_MAP in the GILDAS/CLASS software package, with a beam size of $160''$ and pixel size of $80''$. A third degree polynomial base-line was usually used to fit each extracted RRL spectrum in the line-free channels of the $V_{\rm LSR}$ range from -80 km s^{-1} to +150 km s^{-1} for subtraction. Examples of the observed RRL spectra for the HII region G49.204−0.345 are given in Figure 1. The signal to noise ratio (S/N) of the H101α spectrum is low, because it (6289.144 MHz) is close to the boundary of the effective bandpass (∼ 6300 MHz − 7400 MHz).

Averaging the simultaneously observed RRL spectra could significantly improve sensitivity for detecting ionized gas (e.g., Balser 2006; Anderson et al. 2011; Liu et al. 2013; Alves et al. 2015). According to Menzel (1968), the oscillator strengths for RRLs we observed only differ by $\lesssim 5\%$ for transitions H101α to H96α in similar physical conditions, so that their line widths and velocities should resemble each other. To first order, it is therefore reasonable to average these transitions together to get a higher quality stacked RRL spectrum (e.g., see Fig. 1). We first gridded the data of each observed RRL by using XY_MAP in the CLASS software package with the same beam size of $160''$ and pixel size of $80''$, then, for each pixel in the mapped area, the spectra of six RRLs were resampled to the same velocity resolution of 4.4 km s^{-1}, and stacked together by averaging the spectra weighted by their spectral root mean square (rms) noise. Here the rms was estimated by using the data in the line-free channels of each extracted spectrum in the $V_{\rm LSR}$ range from -80 km s^{-1} to $+150$ km s^{-1}. The S/N of the stacked line is higher than the individual RRL by a factor of about $\sqrt{6}$. The map for integrated intensity of the stacked RRL ($\int T_{\rm MB} dV_{\rm LSR}$) is shown in Figure 2. No beam corrections were applied to the data.

3 RESULTS AND DISCUSSIONS

The region we mapped has been covered by the HIPASS/ZOA RRL survey (Alves et al. 2010, 2015) at 1.4 GHz for observations of H166α, H167α and H168α transitions with an angular resolution of about $14.4'$. For comparison, we made the integrated intensity map by using the data from the HIPASS 1.4 GHz RRL survey in the same area as ours.

Figure 3 also shows the smoothed TMRT 6 GHz RRL map with the same resolution as the HIPASS/ZOA RRL survey. The emission features given by our pilot observations and the HIPASS survey are consistent with each other. In the maps, there are three obvious emission features near ($l \sim 48.5^\circ$, $b \sim 0.1^\circ$), ($l \sim 49.0^\circ$, $b \sim -0.3^\circ$) and ($l \sim 49.5^\circ$, $b \sim -0.3^\circ$). They have been grouped into two star forming complexes, G48.6+0.1 and G49.5−0.3, by Russeil (2003). As shown in Figure 2, one can identify many more details from the 65-m TMRT observations because the resolution ($\sim 2.7'$) is about five times higher than the HIPASS/ZOA survey. The line ratios of the 6 GHz RRLs and the 1.4 GHz RRLs for re-

[2] *https://www.iram.fr/IRAMFR/GILDAS/*

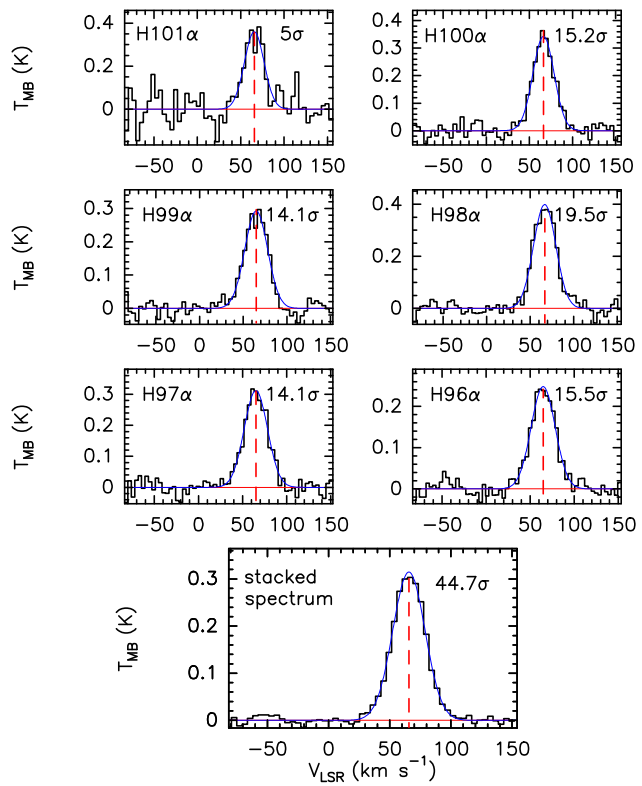

Fig. 1 Examples of RRL (H101α, H100α, H99α, H98α, H97α and H96α) spectra toward the HII region G49.204−0.345 with Gaussian fits for deriving line parameters. The stacked spectrum is shown in the *bottom panel*. The centroid velocities are marked by vertical dashed lines. The σ shown in each panel is the spectrum rms, which was estimated by using the data points in the line-free channels of the extracted spectrum, which has a $V_{\rm LSR}$ range from $-80\,{\rm km\,s^{-1}}$ to $+150\,{\rm km\,s^{-1}}$.

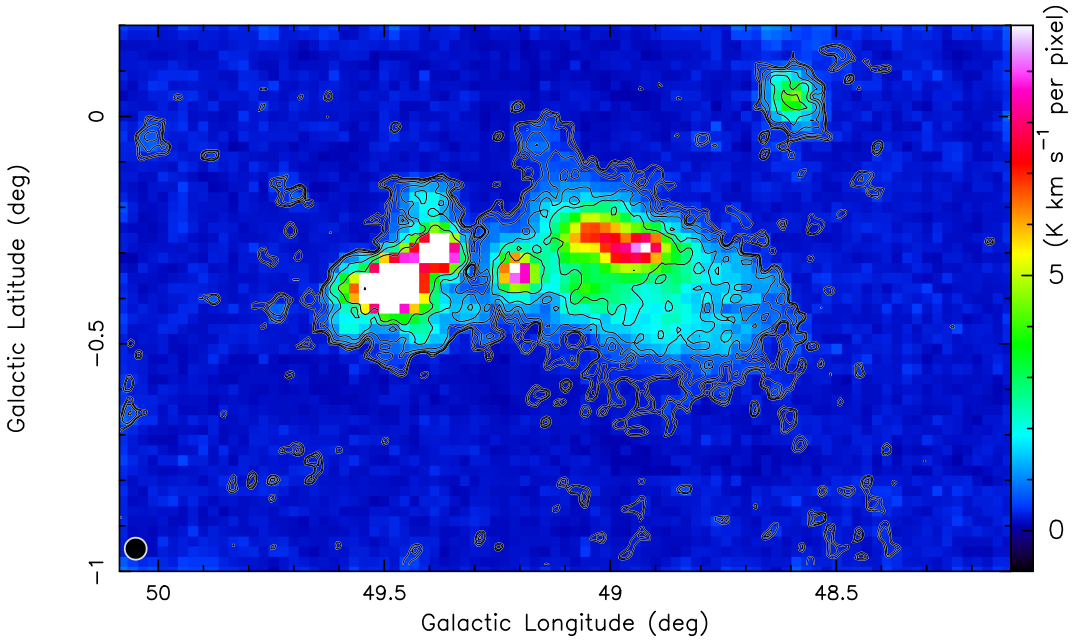

Fig. 2 Integrated RRL intensity map obtained by the TMRT observations, overlaid with contours for the spectrum S/N of 2.5σ, 3σ, 4σ, 6σ, 10σ and 18σ for the stacked line. Here, σ is the rms of the stacked spectrum in each pixel, which was estimated by using the data in the line-free channels of the stacked spectrum. The typical value of σ is about 9 mK ($T_{\rm MB}$, see Table 2). The beam size for the stacked data ($160''$) is indicated by a black filled circle in the lower-left corner.

Table 2 Summary of RRL Survey Parameters by the TMRT

RRLs:	Rest Freq. (MHz)	Beam FWHM ($'$)	Vel. resolution (km s^{-1})	$\sigma_{\rm mean}{}^{\dagger}$ ($T_{\rm MB}$, mK)
H101α	6289.144	2.57	4.4	51
H100α	6478.760	2.50	4.2	16
H99α	6676.076	2.42	4.1	16
H98α	6881.486	2.35	4.0	18
H97α	7095.411	2.27	3.9	16
H96α	7318.296	2.20	3.8	13
stacked		2.67	4.4††	9
Polarizations			Dual circular	
Longitude coverage			$l = 48.1^{\circ} - 50.1^{\circ}$	
Latitude coverage			$b = -1.0^{\circ} - 0.2^{\circ}$	
Gridded beam FWHM			$160''$	
Gridded pixel size			$80''$	

Notes: "†" means spectral rms noise for the mapped region. The spectral rms noise was estimated by using data in the line-free channels of the extracted spectrum for each gridded pixel; "††" corresponds to the frequency of the H101α line.

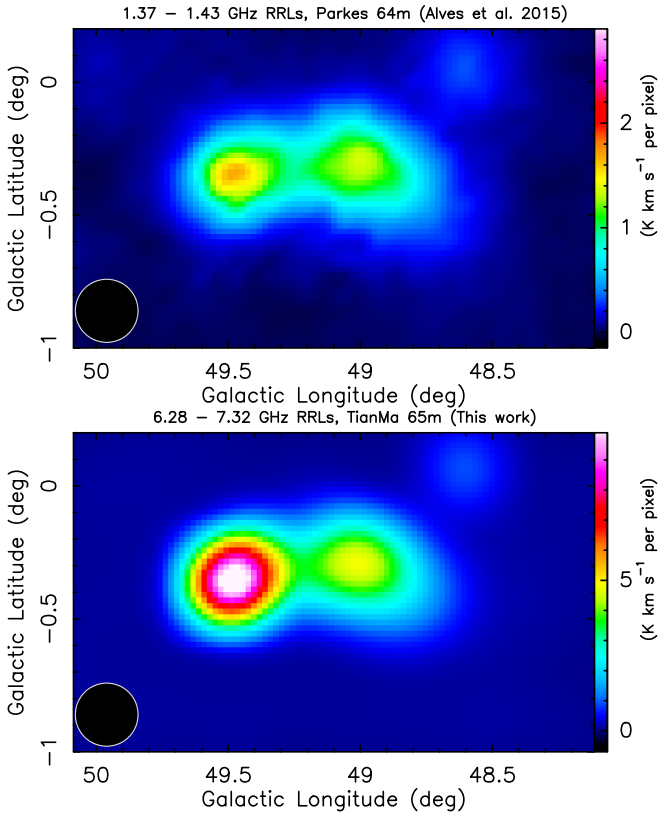

Fig. 3 *Left:* the integrated intensity map of the stacked 1.4 GHz RRLs (H166α, H167α and H168α) that we made by using the data from the HIPASS survey (Alves et al. 2015). The beam size of $14.4'$ is indicated by a black filled circle in the lower-left corner. *Right:* same as Fig. 2, but smoothed to the same resolution as the HIPASS survey.

gions near ($l \sim 49.0^{\circ}$, $b \sim -0.3^{\circ}$) and ($l \sim 49.5^{\circ}$, $b \sim -0.3^{\circ}$) are different, indicating different physical processes in the ISM. Sophisticated analysis and/or modeling would be necessary to reveal the physical properties in these ionized gas clouds.

In this sky area, there are 24 known HII regions with RRL measurements and one additional Sharpless HII region (SH 2−79 = G48.97−0.55) with only optical Hα detection (see Table A.1). We extracted their RRL spectra within one beam area ($160''$) from our

stacked RRL data and obtained 21 of them detected with a spectral S/N greater than 3σ (see Fig. A.1). The other four HII regions, G49.738−0.616 (Bania et al. 2012), G49.998−0.125a, G49.998−0.125b (Anderson et al. 2011) and G50.039−0.274 (Bania et al. 2012), have an S/N less than 3σ. They were detected by simultaneous targeted pointing observations of four to seven RRLs by the Arecibo 300-m telescope (Bania et al. 2012) or GBT 100-m telescope (Anderson et al. 2011), which also have much longer on source integration time (e.g., $\sim$ 6 minutes, Anderson et al. 2011) than our survey observations ($\sim$ 0.67 minutes per one beam area).

A Gaussian was fitted to the stacked RRL spectrum for deriving line parameters (see Table A.1). The centroid velocity $V_{\rm LSR}$ and the full width at half maximum (FWHM) line width ΔV we obtained for the 21 HII regions are compared with those given in the literature as shown in Figure 4. For the HII regions having more than one measurement of $V_{\rm LSR}$ or ΔV in the literature (see Table A.1), we adopted the mean value ($V_{\rm LSR} = \Sigma\frac{V_i}{N}$ or $\Delta V = \Sigma\frac{\Delta V_i}{N}$). We found that the measured $V_{\rm LSR}$ by TMRT is well correlated with those given in references, with a Spearman rank correlation coefficient of 0.93. The best linear least-squares fit has a slope of 1.01 ± 0.01 and a y-axis intercept of 0.65 ± 0.53, which do not deviate significantly from the equal line (see Fig. 4). The measurement of line centroid velocity $V_{\rm LSR}$ seems not to be influenced significantly by the observed RRL frequencies and the telescope used, which can also be seen from data collected in Table A.1. The deviations of $V_{\rm LSR}$ given by different research works for an HII region are always less than 7 km s^{-1}.

For the FWHM line width ΔV, values given by the TMRT are moderately correlated with those given by references, with a Spearman rank correlation coefficient of 0.61. The best linear least-squares fit to the 21 HII regions has a slope of 0.93 ± 0.10 and a y-axis intercept of 3.73 ± 2.54, which indicates that values ΔV given by the TMRT observations are in general slightly narrower than those given by references. As shown in Table A.1, a large number of ΔV from references were obtained by observing RRL(s) with principal quantum number $n \geqslant 109$, which are higher than what are used in our observations. Theoretically, due to the Stark broadening effect, the FWHM line widths of RRLs will increase systematically with principal quantum number n (Smirnov et al. 1984, Gordon & Sorochenko 2009). But in observations, things become complex. Unlike the line centroid velocity, the measurements of line width are sensitive to the spectral S/N. For the RRL spectrum with a low S/N, the weak and broad line wing will be hard to differentiate from the underlying continuum emission, hence, the fitted FWHM line width may be narrower than the true value. In addition, the line width measurements are also influenced by the observed RRL frequencies and the telescope used. As shown in Table A.1, the line widths of RRLs are in the range from 16 km s^{-1} to $\sim$40 km s^{-1}. The deviations of line width for an HII region given by different research works could sometimes be as large as more than 10 km s^{-1}. In the plot of the line width ΔV (Fig. 4), one may notice an "outlier" SH 2−79 (G48.97−0.55), which only has optical $H\alpha$ detection in the literature. The measured line width $\Delta V_{\rm H\alpha}$ (41.5 ± 2.4 km s^{-1}, Fich et al. 1990) is significantly larger than $\Delta V_{\rm RRL}$ (23.7 ± 2.7 km^{-1}). Fich et al. (1990) first found that $\Delta V_{\rm H\alpha}$ is systematically broader than $\Delta V_{\rm RRL}$ for some HII regions. Anderson et al. (2015) confirmed the finding of Fich et al. (1990), and found that $\Delta V_{\rm H\alpha} - \Delta V_{\rm RRL}$ could be as large as 20 km^{-1} for some HII regions. However, the reason is still not clear (Fich et al. 1990, Anderson et al. 2015).

Anderson et al. (2014) has identified $\sim$8000 HII regions or candidates by using survey data from the all-sky Wide-field Infrared Survey Explorer (WISE) satellite. About 6 000 of them still do not have RRL measured. In the region we mapped, there are 107 WISE HII regions or candidates, and their RRL spectra can be extracted from our data. Some targets are very close to each other, with angular separation less than the beam of TMRT, and hence cannot be resolved by our observations. The 107 sources were grouped and finally we obtained 72 targeted positions. The RRL spectra within one beam ($160''$) for these target positions were extracted, and there are 45 target positions having spectral S/N greater than 5σ, and 30 of them are new detections (see Fig. A.2). The line parameters for these 30 new detections of RRLs are measured and listed in Table A.2.

Most of the 21 known HII regions and 30 new WISE HII regions coincide with the star forming complexes G48.6+0.1 and G49.5−0.3. Outside these two complexes, more than 90 positions with a spectral S/N $> 2.5\sigma$ (see Fig. 2) are present, and they may be candidates of new RRL sources. The RRL spectra within one beam from the targeted positions were extracted from the stacked RRL data. We found that there are 25 sources with a spectral S/N $> 5\sigma$ (Fig. A.3), but which are not included in the catalogs of known HII regions with RRL detections (e.g., Anderson et al. 2011; Bania et al. 2012; Hou & Han 2014, Anderson et al. 2015). The measured line parameters are given in Table A.3. We made cross-identifications by using the position coincidence for SIMBAD objects with a searching radius of $160''$, and

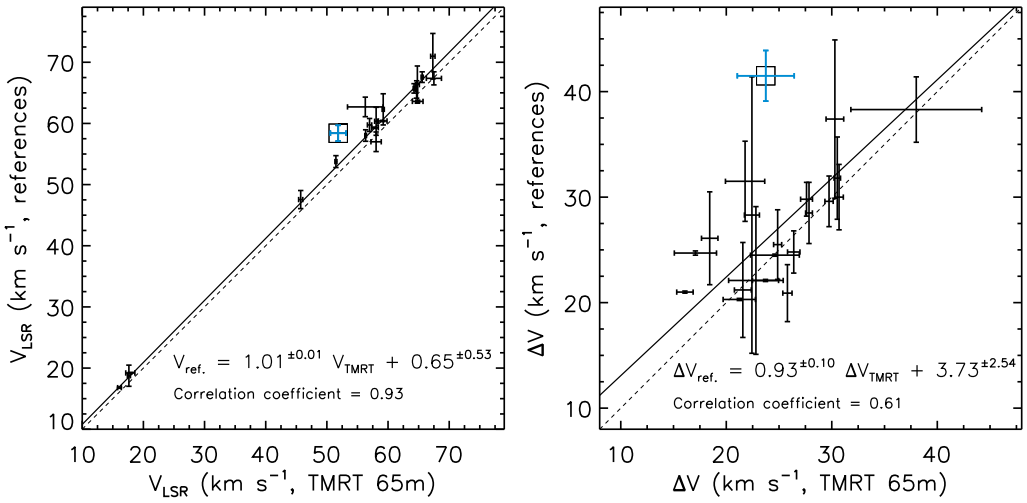

Fig. 4 Comparisons of the centroid velocity $V_{\rm LSR}$ (*left*) and the FWHM line width ΔV (*right*) measured by the TMRT 65-m with those from references (see Table A.1). The 1σ errors for $V_{\rm LSR}$ and ΔV are plotted as error bars. In each panel, the solid line indicates the best linear least-squares fit to the data, and the dashed line is the equal line. The Spearman rank correlation coefficient is also given in each panel. Except for SH 2−79 (G48.97−0.55), which only has optical Hα observations in the literature and is marked by a square, other HII regions shown in the plot all have RRL detections in the literature.

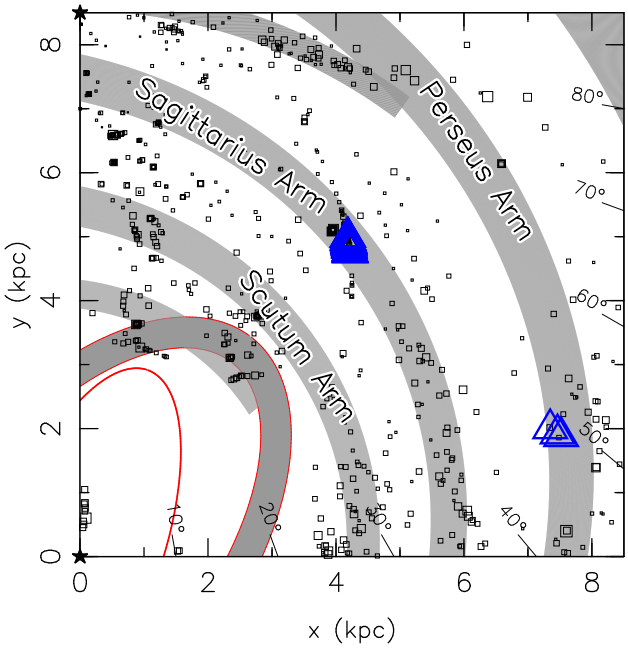

Fig. 5 Distributions of the 44 new RRL sources (*blue triangles*) projected into the Galactic plane, overlaid with a spiral arm model (see fig. 5 in Hou & Han 2014) to show the known spiral arm segments. The locations of the GC ($x = 0$ kpc, $y = 0$ kpc) and the Sun ($x = 0$ kpc, $y = 8.5$ kpc) are indicated by black stars. The known HII regions are marked by black squares. To estimate the distances, the IAU standards of $R_0 = 8.5$ kpc, $\Theta_0 = 220$ km s^{-1} and standard solar motions were adopted.

probable objects are listed in Table A.3. G48.39−0.91, G48.45−0.92 and G48.50+0.13 coincide with *Spitzer* infrared bubbles (Simpson et al. 2012). G49.10−0.59 and G49.20+0.02 coincide with Young Stellar Objects (Kang et al. 2009; Spitzer Science 2009), which suggests that they are HII regions.

With the $V_{\rm LSR}$ measured for these newly detected RRL sources, we can estimate their kinematic distances, which depend on the adopted Galaxy fundamental pa-

rameters and the solution to the kinematic distance ambiguity (e.g., Hou et al. 2009). How to determine the exact values of Galaxy fundamental parameters R_0, Θ_0 and solar motions[3] with respect to the Local Standard of Rest (LSR) are outstanding questions. Besides the IAU standards for the distance of the Sun to the Galactic Center (GC) $R_0 = 8.5$ kpc, the circular orbital speed at the Sun $\Theta_0 = 220$ km s^{-1}, and solar motions with respect to the LSR, i.e., $U_\odot = 10.27\,\mathrm{km\,s^{-1}}$, $V_\odot = 15.32\,\mathrm{km\,s^{-1}}$ and $W_\odot = 7.74\,\mathrm{km\,s^{-1}}$, another set of Galaxy parameters was recommended in recent research studies (see the discussions in Hou & Han 2014 for details). They are $R_0 = 8.3\,\mathrm{kpc}$, $\Theta_0 = 239\,\mathrm{km\,s^{-1}}$ (e.g., Brunthaler et al. 2011; Reid et al. 2014), and the solar motions of Schönrich et al. (2010) with $U_\odot = 11.10\,\mathrm{km}\ ^{-1}$, $V_\odot = 12.24\,\mathrm{km\,s^{-1}}$ and $W_\odot = 7.25\,\mathrm{km\,s^{-1}}$. We noticed that most of these 55 new RRL sources have $V_{\rm LSR}$ close to the tangent point speeds (~ 55 km s^{-1}).

For the first step, we try to identify the RRL sources located near the tangent points. According to the criteria of Reid et al. (2009), we made the identification by using two different sets of fundamental Galaxy parameters, i.e., the IAU standards and $R_0 = 8.3\,\mathrm{kpc}$, $\Theta_0 = 239\,\mathrm{km\,s^{-1}}$ and the solar motions of Schönrich et al. (2010). If consistent results were obtained by using the two different sets of Galaxy parameters, we place the RRL source at the tangent point. We found that 41 sources are located at the tangent points. For the other three RRL sources, we resolved the kinematic distance ambiguity by using the HI emission/absorption method and the HI self-absorption method as described in Anderson & Bania (2009). The distance parameters for these 44 RRL sources were then calculated by using a flat rotation curve (Reid et al. 2014) and are listed in Tables A.2 and A.3. As shown in Figure 5, they are located in the Sagittarius Arm and the Perseus Arm.

4 CONCLUSIONS

We conducted a pilot survey of RRLs toward a $2^\circ \times 1.2^\circ$ sky area near the Sagittarius Arm tangent with the newly constructed TMRT. Six hydrogen RRLs (H96α−H101α) were recorded simultaneously. The spectra of these transitions were first resampled to a velocity resolution of 4.4 km s^{-1} and then stacked together by using a weighted mean to improve the detection of the RRLs from the ionized clouds.

We showed that the major emission components in the integrated intensity map (Fig. 2) are consistent with the previous low-resolution map of 1.4 GHz RRLs. We measured the line parameters for 21 known HII regions and found that the centroid velocities are consistent with previous results. The higher resolution of this new pilot survey enables us to see detailed emission features in the area. In the region with more than 80 WISE selected HII region candidates, we obtained stacked RRLs for 30 positions with a spectral S/N greater than 5σ. We also identified 25 new discrete sources with stacked RRL S/N greater than 5σ. Among the 55 newly detected RRL sources, we estimated the distances for 44 of them. They are located in the Sagittarius Arm and the Perseus Arm. In this targeted region of only $\sim 2^\circ \times 1.2^\circ$, we have detected RRLs for 55 targets for the first time. The results suggest that the 65-m TMRT has the ability to map and study Galactic ionized gas.

Acknowledgements We thank the anonymous referee for instructive suggestions/comments, which helped us to improve the paper. We thank the kind assistance of the TMRT operators at Shanghai Astronomical Observatory of the Chinese Academy of Sciences during the observations. The authors are supported by the National Natural Science Foundation of China (11303035, 11473034, 11503033 and 11503070). J.L. Han is also supported by the Key Research Program of the Chinese Academy of Sciences, Grant No. QYZDJ-SSW-SLH021. X.Y.G. is additionally supported by the FAST Fellowship and by the Young Researchers Grant of National Astronomical Observatories, Chinese Academy of Sciences. The FAST Fellowship is supported by Special Funding for Advanced users, budgeted and administered by the Center for Astronomical Mega-Science, Chinese Academy of Sciences (CAMS). LGH thanks Dr. Xi Chen, Zhi-Yu Zhang, Jin-Long Xu and Chuan-Peng Zhang for their kind and helpful suggestions/comments in the data reduction. This research has made use of the SIMBAD database, operated at CDS, Strasbourg, France (Wenger et al. 2000).

Appendix A: HII REGIONS AND THEIR RRLS

Here we present the RRLs for 21 known HII regions (Fig. A.1 and Table A.1) and the newly detected RRLs for WISE HII region candidates at 30 positions (Fig. A.2 and Table A.2) together with 25 new RRL sources (Fig. A.3 and Table A.3).

[3] In the Doppler tracking system of TMRT, standard solar motions were adopted.

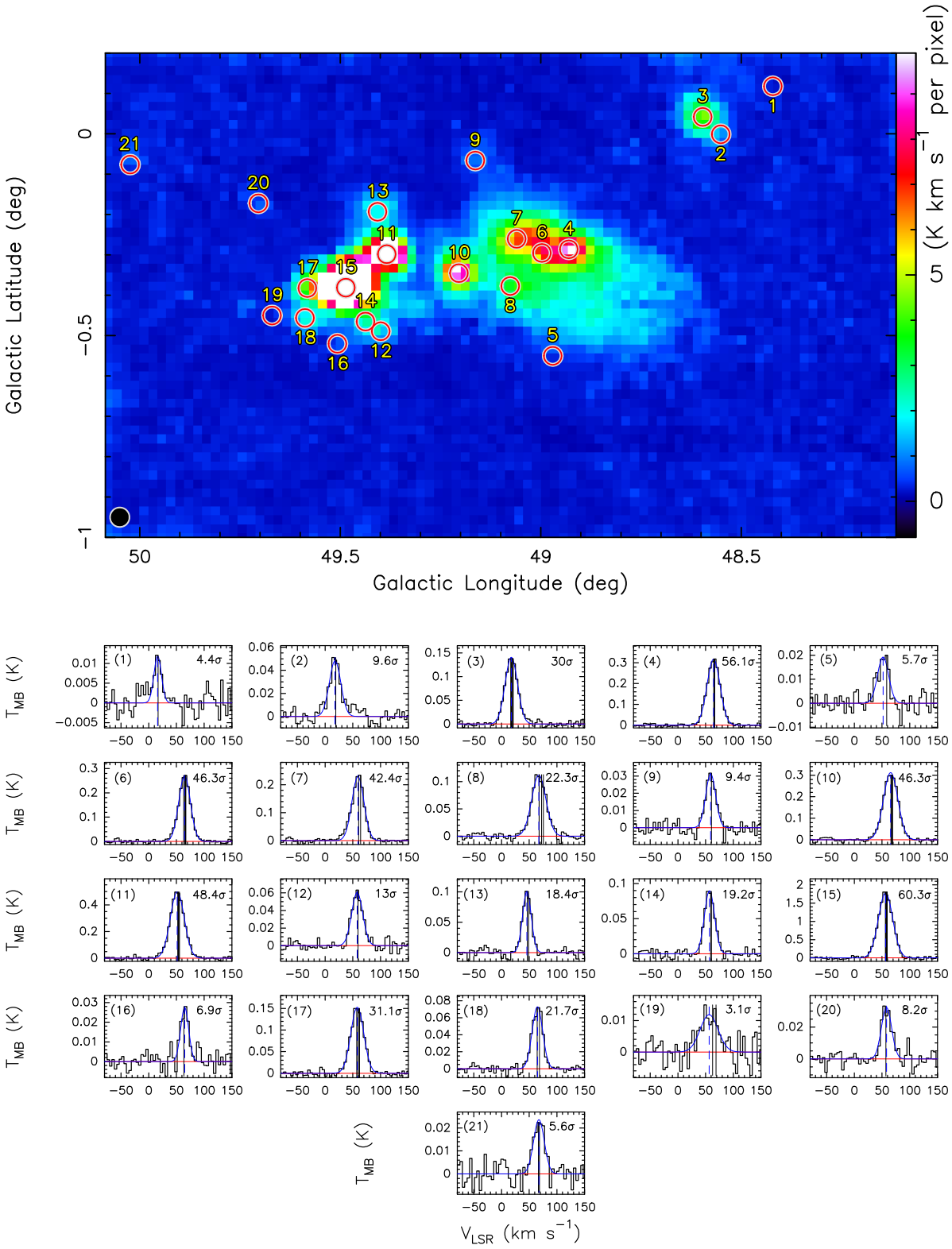

Fig. A.1 21 known HII regions are circled in the survey area in the *upper panel*, and their stacked RRL spectra are presented in the *lower panels*. A Gaussian fit indicated by a solid line is used for deriving line parameters. The centroid velocities are marked by vertical dashed lines and are compared with those in references as indicated by vertical solid lines.

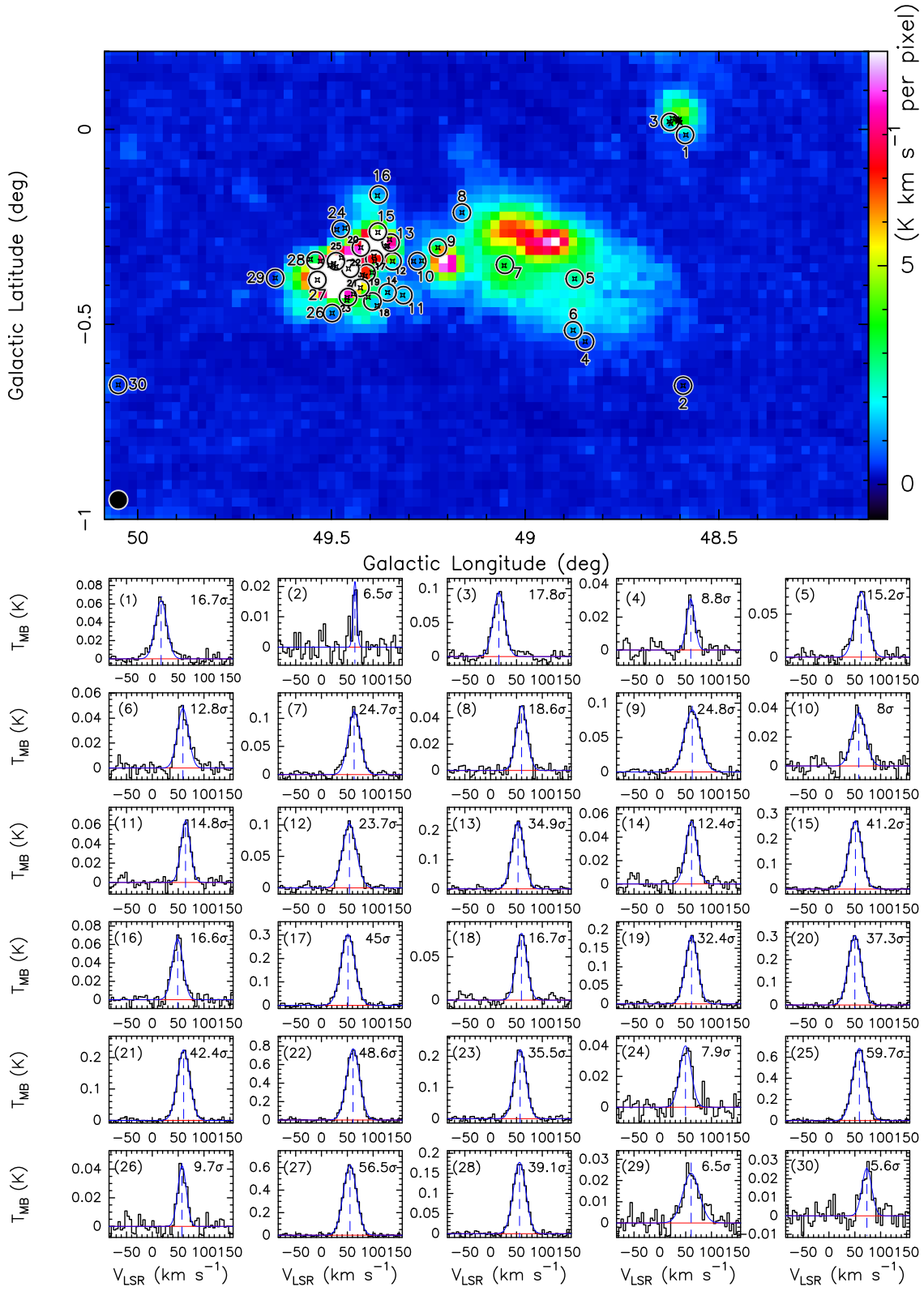

Fig. A.2 30 target positions (*circles*) toward the WISE HII region candidates (*crosses*) are marked in the survey area. Their stacked RRL spectra are fitted with a Gaussian (*blue solid line*) for the line parameter derivation, as shown in the *lower panels*. The centroid velocities are marked by vertical dashed lines.

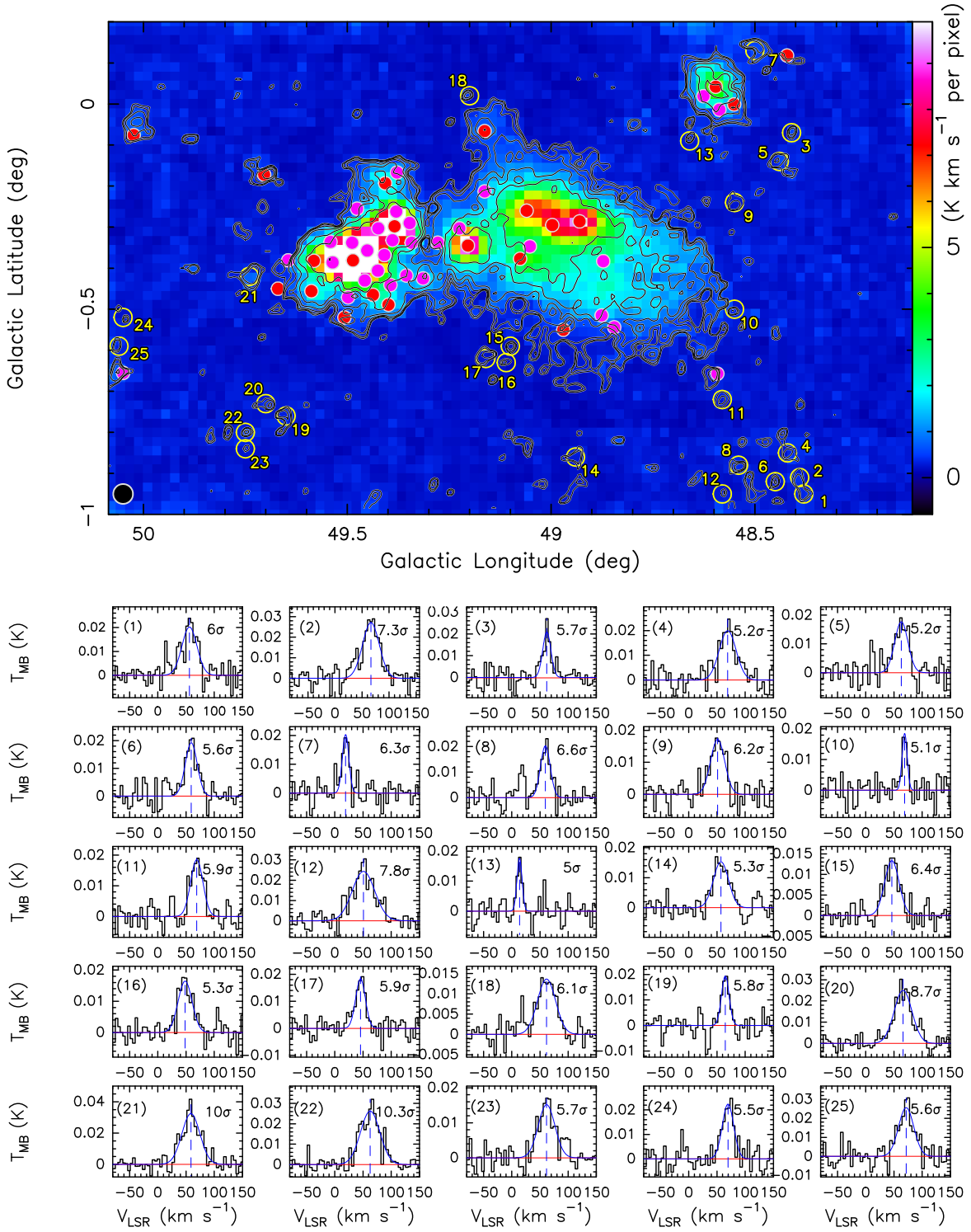

Fig. A.3 25 new RRL sources (circles) are identified in the survey region (see the *upper panel*) and their stacked RRL spectra are fitted with a Gaussian (*blue solid line*) for deriving line parameters. The centroid velocities are indicated by vertical dashed lines. The 21 known HII regions (*filled red circles*) and the 30 targeted positions of WISE HII region candidates (*filled pink circles*) are also indicated. Contours shown in the *upper panel* are the same as those in Fig. 2.

Table A.1 Line Parameters for the 21 Known HII Regions

No.	l	b	Ref.	$V_{\rm LSR}$	$\delta V_{\rm LSR}$	ΔV	$\delta\Delta V$	line(s) observed	Ref.	$V_{\rm LSR}$	$\delta V_{\rm LSR}$	ΔV	$\delta\Delta V$	$\int T_{\rm MB}dV$	$\delta\int T_{\rm MB}dV$
	(°)	(°)		(km s^{-1})						(km s^{-1})				(K km s^{-1})	
(1)	(2)	(3)	(4)	(5)	(6)	(7)	(8)	(9)	(10)	(11)	(12)	(13)	(14)	(15)	(16)
1	48.421	0.118	abbr11	16.8	0.1	21.0	0.1	H87–93α	abbr11	16.1	0.3	16.1	0.8	0.20	0.01
2	48.551	−0.001	abbr11	19.2	0.1	24.5	0.1	H87–93α	abbr11	17.9	0.7	24.6	2.3	1.26	0.09
3	48.596	0.042	dwbw80	17.5	5.0	24.	5.0	H110α	dwbw80	17.6	0.2	26.4	0.6	3.96	0.08
				17.2	1.0	27.7	2.2	H87+88/85α	lock89						
				17.0	1.4	26.6	2.5	H109α	rwb+70						
				21.1	2.0	23.1	3.6	H109α	wmgm70						
				20.8	0.8	26.0	2.0	H76α	wwb83						
				18.1	0.4	23.7	1.0	H110α	ahck02						
				19.58	1.20	22.52	2.52	H110α	dze+11						
4	48.930	−0.286	dwbw80	66.0	5.0	27.	5.0	H110α	dwbw80	64.2	0.1	27.8	0.3	9.38	0.09
				66.5	0.6	29.6	1.3	H87+88/85α	lock89						
				66.4	1.6	33.4	3.0	H109α	wmgm70						
				66.0	0.8	30.5	1.5	H76α	wwb83						
				64.77	0.59	27.90	1.44	H110α	hze+11						
				64.55	0.50	24.73	1.21	H110α	dze+11						
				65.86	0.06	26.74	0.17	H91α	qrbb06						
5	48.97	−0.55	bfs82	58.4	1.3	41.5	2.4	Hα	fdt90	51.9	1.3	23.7	2.7	0.49	0.05
6	48.997	−0.295	lock89	65.5	1.5	27.7	2.0	H87+88/85α	lock89	64.7	0.2	24.9	0.4	7.13	0.09
				63.2	1.2	25.6	1.2	H109α	rwb+70						
				65.8	1.4	29.3	2.4	H109α	wmgm70						
				66.4	3.0	20.6	2.7	H109α	mh67						
				66.86	0.05	24.43	0.16	H91α	qrbb06						
7	49.060	−0.260	dwbw80	60.5	5.0	19.	5.0	H110α	dwbw80	59.2	0.2	25.8	0.4	6.28	0.09
				64.1	1.3	22.8	3.0	H87+88/85α	lock89						
8	49.076	−0.377	dwbw80	68.0	5.0	40.	5.0	H110α	dwbw80	67.3	0.4	30.3	0.8	3.61	0.09
				67.9	0.8	32.2	2.0	H87+88/85α	lock89						
				72.4	2.8	46.9	5.4	H109α	wmgm70						
				75.6	0.9	30.6	2.2	H76α	wwb83						
9	49.163	−0.066	abbr11	60.4	0.1	20.3	0.1	H87–93α	abbr11	59.1	0.7	21.2	1.5	0.70	0.05
10	49.204	−0.345	dwbw80	67.2	5.0	32.	5.0	H110α	dwbw80	65.6	0.2	30.7	0.4	10.19	0.12
				67.2	1.0	24.5	2.4	H87+88/85α	lock89						
				67.2	1.4	30.7	3.0	H109α	rwb+70						
				66.1	1.8	35.1	3.0	H109α	wmgm70						
				69.1	0.4	30.2	1.0	H76α	wwb83						
				67.9	0.1	29.3	0.2	H110α	swa+04						
				68.1	0.1	27.9	0.4	H110α	was+03						
				67.79	0.05	30.32	0.15	H91α	qrbb06						

Notes: Column (1) is the sequential number for each HII region, corresponding to those in Figure A.1; Columns (2) and (3) are the Galactic longitude and latitude respectively with the associated reference given in Column (4); Columns (5) to (8) are the line parameters given by the references in Column (10). The line parameters include the centroid velocity, its 1σ uncertainty, the FWHM line width and its 1σ uncertainty. The line(s) observed are listed in Column (9). Columns (11) to (16) are the line parameters measured by using TMRT. Columns (11) and (12) list the centroid velocity and its 1σ uncertainty; Columns (13) and (14) give the FWHM line width and its 1σ uncertainty; Columns (15) and (16) are the integrated intensity of the stacked line and its uncertainty.

References: abbr11: Anderson et al. (2011); ahck02: Araya et al. (2002); brba11: Balser et al. (2011); bfs82: Blitz et al. (1982); cmh74: Churchwell et al. (1974); dwbw80: Downes et al. (1980); dze+11: Du et al. (2011); fdt90: Fich et al. (1990); hze+11: Han et al. (2011); lock89: Lockman (1989); lph96: Lockman et al. (1996); mn81: McGee & Newton (1981); mh67: Mezger & Hoglund (1967); qrbb06: Quireza et al. (2006); rwb+70: Reifenstein et al. (1970); swa+04: Sewilo et al. (2004); st79: Silverglate & Terzian (1979); was+03: Watson et al. (2003); wmgm70: Wilson et al. (1970); wwb83: Wink et al. (1983).

Table A.1 — *Continued.*

No.	l	b	Ref.	$V_{\rm LSR}$	$\delta V_{\rm LSR}$	ΔV	$\delta\Delta V$	line(s) observed	Ref.	$V_{\rm LSR}$	$\delta V_{\rm LSR}$	ΔV	$\delta\Delta V$	$\int T_{\rm MB}dV$	$\delta\int T_{\rm MB}dV$
	(°)	(°)		(km s^{-1})						(km s^{-1})				(K km s^{-1})	
(1)	(2)	(3)	(4)	(5)	(6)	(7)	(8)	(9)	(10)	(11)	(12)	(13)	(14)	(15)	(16)
11	49.384	−0.298	dwbw80	52.5	5.0	31.0	5.0	H110α	dwbw80	51.5	0.2	29.7	0.4	15.74	0.18
				53.7	0.3	28.7	0.7	H87+88/85α	lock89						
				52.8	1.1	29.8	1.8	H109α	wmgm70						
				55.4	0.4	29.4	0.9	H76α	wwb83						
				53.71	0.59	32.82	1.41	H110α	hze+11						
				54.46	0.75	25.55	1.66	H110α	dze+11						
				53.76	0.03	28.44	0.07	H91α	qrbb06						
12	49.399	−0.489	abbr11	59.3	0.1	22.1	0.1	H87–93α	abbr11	57.9	0.5	23.7	1.2	1.52	0.07
13	49.407	−0.193	dwbw80	46.5	5.0	23.0	5.0	H110α	dwbw80	45.7	0.3	18.4	0.8	1.97	0.07
				48.6	3.0	29.2	4.1	H87+88/85α	lock89						
14	49.437	−0.465	dwbw80	59.0	5.0	18.0	5.0	H110α	dwbw80	57.0	0.4	21.6	0.8	2.06	0.07
				60.5	0.8	24.3	1.8	H87+88/85α	lock89						
15	49.486	−0.381	dwbw80	57.1	2.0	30.0	2.0	H110α	dwbw80	56.3	0.1	30.5	0.3	57.76	0.51
				58.2	0.3	30.2	0.4	H87+88/85α	lock89						
				58.2	0.2	32.1	0.6	H109α	rwb+70						
				59.0	1.0	37.2	1.8	H109α	wmgm70						
				57.2	0.1	30.7	1.1	H76α	wwb83						
				55.95	0.01	30.16	0.03	H87–93α	brba11						
				58.7	0.5	32.0	2.0	H109α	cmh74						
				58.33	0.27	26.84	0.60	H110α	hze+11						
				57.3	0.03	29.5	0.1	H76α	mn81						
				59.1	2.1	41.6	2.5	H109α	mh67						
				58.71	0.03	30.87	0.06	H91α	qrbb06						
				58.40	0.02	30.57	0.04	H91α	qrbb06						
16	49.507	−0.520	abbr11	63.6	0.2	24.7	0.2	H87–93α	abbr11	64.9	0.9	17.1	2.0	0.50	0.05
17	49.582	−0.382	dwbw80	62.0	5.0	27.0	5.0	H110α	dwbw80	58.1	0.2	27.6	0.6	4.49	0.08
				62.1	2.4	30.3	3.3	H87+88/85α	lock89						
				61.7	0.9	30.9	2.3	H76α	wwb83						
				58.98	0.44	30.95	0.99	H110α	dze+11						
				56.96	0.04	29.73	0.11	H91α	qrbb06						
18	49.588	−0.456	dwbw80	68.5	5.0	19.0	5.0	H110α	dwbw80	64.8	0.3	22.4	0.7	1.74	0.05
				64.2	2.2	37.5	3.0	H87+88/85α	lock89						
19	49.67	−0.45	was+03	62.7	1.6	38.3	3.1	H110α	was+03	56.3	2.9	38.0	6.2	0.48	0.07
20	49.704	−0.172	lph96	57.0	1.6	31.5	3.8	H109-110α	lph96	58.0	0.8	21.8	1.9	0.75	0.06
21	50.024	−0.076	lock89	66.8	0.8	16.4	1.8	H87+88/85α	lock89	67.5	1.2	22.8	2.6	0.57	0.06
				66.7	0.8	30.0	2.0	H167α	st79						
				68.6	0.6	20.0	1.0	H140α	st79						

Table A.2 RRL parameters for the 30 positions of WISE HII region candidates that we measured in this work.

No.	l	b	WISE sources	$V_{\rm LSR}$	$\delta V_{\rm LSR}$	ΔV	$\delta\Delta V$	$\int T_{\rm MB}dV$	$\delta\int T_{\rm MB}dV$	Mark	$D_{8.5}$	$D_{8.3}$
	(°)	(°)		(km s^{-1})				(K km s^{-1})			(kpc)	
(1)	(2)	(3)	(4)	(5)	(6)	(7)	(8)	(9)	(10)	(11)	(12)	(13)
1	48.585	–0.014	G48.585–0.014	17.0	0.4	26.5	1.2	1.79	0.06	kfar	9.95	9.48
2	48.592	–0.657	G48.592–0.657	64.8	0.6	8.4	2.4	0.19	0.04	ktan	5.62	5.49

Notes: Column (1) is the sequential number marked in Fig. A.2; Columns (2) and (3) are the Galactic longitude and latitude of the targeted position respectively; Column (4) lists the WISE HII region candidates; Columns (5) and (6) list the centroid velocity and its 1σ uncertainty respectively; Columns (7) and (8) give the FWHM line width and its 1σ uncertainty respectively; Columns (9) and (10) are the integrated intensity and its uncertainty respectively; Column (11) gives notes for: kfar − the farther kinematic distance is adopted, ktan − the source is located at the tangent point and the distance to the tangent is adopted; Column (12) lists the distance to the Sun which is calculated with a flat rotation curve with the IAU standard $R_0 = 8.5$ kpc, $\Theta_0 = 220\,{\rm km\,s^{-1}}$ and the IAU standard solar motions of $U_\odot = 10.27\,{\rm km\,s^{-1}}$, $V_\odot = 15.32\,{\rm km\,s^{-1}}$ and $W_\odot = 7.74\,{\rm km\,s^{-1}}$; Column (13) is the same as Column (12), except with $R_0 = 8.3$ kpc, $\Theta_0 = 239\,{\rm km\,s^{-1}}$ (Reid et al. 2014) and the solar motions of $U_\odot = 11.10\,{\rm km\,s^{-1}}$, $V_\odot = 12.24\,{\rm km\,s^{-1}}$ and $W_\odot = 7.25\,{\rm km\,s^{-1}}$ (Schönrich et al. 2010).

Table A.2 — *Continued.*

No.	l	b	WISE sources	$V_{\rm LSR}$	$\delta V_{\rm LSR}$	ΔV	$\delta\Delta V$	$\int T_{\rm MB}dV$	$\delta\int T_{\rm MB}dV$	Mark	$D_{8.5}$	$D_{8.3}$
	(°)	(°)		(km s^{-1})				(K km s^{-1})			(kpc)	
(1)	(2)	(3)	(4)	(5)	(6)	(7)	(8)	(9)	(10)	(11)	(12)	(13)
3	48.626	0.019	G48.600+0.018	16.0	0.4	26.3	1.0	2.64	0.08	kfar	10.02	9.54
			G48.600+0.018									
			G48.602+0.026									
			G48.604+0.023									
			G48.605+0.021									
			G48.606+0.024									
			G48.609+0.027									
			G48.620+0.028									
			G48.624+0.015									
			G48.628+0.020									
			G49.288−0.338									
4	48.845	−0.544	G48.845–0.544	59.9	0.8	18.5	2.0	0.61	0.05	ktan	5.59	5.46
5	48.872	−0.383	G48.872–0.383	62.6	0.5	29.7	1.3	2.39	0.09	ktan	5.59	5.46
6	48.876	−0.515	G48.876–0.515	59.1	0.6	25.4	1.4	1.29	0.06	ktan	5.59	5.46
7	49.054	−0.349	G49.054−0.349	63.4	0.3	27.8	0.8	3.29	0.08	ktan	5.57	5.44
8	49.163	−0.213	G49.163−0.213	60.0	0.4	24.8	0.9	1.29	0.04	ktan	5.56	5.43
9	49.225	−0.303	G49.225−0.303	62.8	0.4	36.2	0.8	3.48	0.07	ktan	5.55	5.42
10	49.278	−0.338	G49.267−0.337	57.8	1.0	31.0	2.5	1.20	0.08	ktan	5.55	5.41
11	49.316	−0.425	G49.316−0.425	64.4	0.5	21.4	1.0	1.46	0.06	ktan	5.54	5.41
12	49.342	−0.338	G49.342−0.338	54.1	0.3	31.6	0.8	3.42	0.07	ktan	5.54	5.41
13	49.347	−0.290	G49.350−0.282	53.1	0.2	27.5	0.5	6.69	0.11	ktan	5.54	5.41
			G49.355−0.298									
			G49.358−0.300									
14	49.355	−0.418	G49.355−0.418	61.2	0.6	26.0	1.5	1.48	0.07	ktan	5.54	5.41
15	49.380	−0.264	G49.380−0.264	51.1	0.2	29.4	0.5	8.54	0.11			
16	49.381	−0.170	G49.381−0.170	49.0	0.4	24.2	1.0	1.70	0.06			
17	49.389	−0.332	G49.388−0.338	51.3	0.2	31.6	0.4	10.20	0.12			
			G49.390−0.325									
18	49.394	−0.441	G49.382−0.452	59.7	0.4	24.7	1.0	2.04	0.07	ktan	5.53	5.40
			G49.405−0.430									
19	49.409	−0.368	G49.395−0.367	61.5	0.2	27.6	0.6	5.38	0.09	ktan	5.53	5.40
			G49.413−0.376									
			G49.420−0.373									
20	49.424	−0.303	G49.424−0.303	49.9	0.2	29.8	0.5	9.66	0.14			
21	49.425	−0.406	G49.425−0.406	60.6	0.2	28.3	0.4	6.77	0.09	ktan	5.53	5.40
22	49.456	−0.357	G49.456−0.357	61.2	0.2	29.5	0.4	24.20	0.25	ktan	5.53	5.40
23	49.457	−0.430	G49.443−0.422	57.2	0.2	26.9	0.5	6.36	0.10	ktan	5.53	5.40
			G49.459−0.431									
			G49.460−0.438									
24	49.476	−0.255	G49.465−0.253	49.7	0.9	26.3	2.1	1.12	0.08			
			G49.486−0.257									
25	49.488	−0.338	G49.474−0.329	58.7	0.1	30.5	0.3	22.18	0.19	ktan	5.52	5.39
			G49.488−0.352									
			G49.494−0.344									
			G49.495−0.348									
			G49.503−0.348									
26	49.498	−0.471	G49.498−0.471	57.5	0.7	19.6	1.5	0.88	0.06	ktan	5.52	5.39
27	49.536	−0.386	G49.536−0.386	55.1	0.1	30.5	0.3	20.19	0.19	ktan	5.52	5.39
28	49.541	−0.336	G49.528−0.338	55.9	0.2	28.6	0.5	5.39	0.08	ktan	5.52	5.39
			G49.554−0.333									
29	49.645	−0.381	G49.645−0.381	60.6	1.4	37.5	3.7	0.93	0.07	ktan	5.50	5.37
30	50.050	−0.655	G50.050−0.655	73.2	1.2	22.2	2.8	0.61	0.07	ktan	5.46	5.33

Table A.3 RRL Parameters for 25 Newly Detected Sources

No.	l	b	$V_{\rm LSR}$	$\delta V_{\rm LSR}$	ΔV	$\delta\Delta V$	$\int T_{\rm MB}dV$	$\delta\int T_{\rm MB}dV$	SIMBAD identification/Ref.	distance	Mark	$D_{8.5}$	$D_{8.3}$
	($^\circ$)	($^\circ$)	(km s^{-1})				(K km s^{-1})			($''$)		(kpc)	
(1)	(2)	(3)	(4)	(5)	(6)	(7)	(8)	(9)	(10)	(11)	(12)	(13)	(14)
1	48.38	−0.95	58.2	1.8	32.8	4.7	0.71	0.08			ktan	5.65	5.51
2	48.39	−0.91	66.5	1.3	36.6	3.5	1.05	0.08	MWP1G048396−009195/(a)	41.8	ktan	5.64	5.51
3	48.41	−0.07	62.1	0.7	17.1	2.4	0.38	0.04			ktan	5.64	5.51
4	48.42	−0.85	69.0	1.7	35.3	5.1	0.75	0.08			ktan	5.64	5.51
5	48.44	−0.14	63.1	1.8	27.6	3.7	0.52	0.06			ktan	5.64	5.51
6	48.45	−0.92	59.3	1.4	25.0	3.4	0.51	0.06	MWP1G048433−009213/(a)	61.3	ktan	5.64	5.51
7	48.50	0.13	19.2	1.0	13.6	2.3	0.29	0.04	MWP1G048507+001330/(a)	27.3	kfar	9.81	9.35
8	48.54	−0.88	59.6	1.3	20.3	3.1	0.44	0.06			ktan	5.63	5.50
9	48.55	−0.24	51.2	1.5	29.5	3.2	0.54	0.05					
10	48.55	−0.50	69.0	0.9	10.5	2.1	0.21	0.04			ktan	5.63	5.49
11	48.58	−0.72	69.1	1.3	25.6	2.6	0.50	0.05			ktan	5.62	5.49
12	48.58	−0.95	50.9	1.2	47.0	2.9	1.22	0.06					
13	48.66	−0.09	13.8	0.9	10.5	2.1	0.20	0.03	IRAS 19187+1348/(b)	52.0			
14	48.94	−0.86	57.1	1.5	31.6	3.0	0.52	0.05	IRAS 19220+1341/(b)	40.7	ktan	5.58	5.45
15	49.10	−0.59	46.4	1.3	30.2	2.8	0.43	0.04	KBP2009 213/(c)	48.8			
16	49.11	−0.63	48.4	1.5	29.2	3.4	0.51	0.05					
17	49.16	−0.62	45.6	1.2	20.3	3.1	0.39	0.05					
18	49.20	0.02	61.7	1.9	38.0	4.6	0.55	0.06	KBP2009 256/(c)	29.1	ktan	5.55	5.42
									2MASS J19214295+1427290/(d)	51.0			
19	49.65	−0.76	64.8	1.2	16.1	2.6	0.33	0.05			ktan	5.50	5.37
20	49.70	−0.73	66.2	1.0	37.2	2.6	0.99	0.06			ktan	5.50	5.37
21	49.74	−0.42	58.7	0.9	37.6	2.0	1.30	0.06			ktan	5.49	5.36
22	49.75	−0.80	62.8	0.9	40.5	2.1	1.13	0.05			ktan	5.49	5.36
23	49.75	−0.84	61.7	1.6	34.9	4.0	0.56	0.05			ktan	5.49	5.36
24	50.05	−0.52	69.6	1.3	23.8	3.2	0.57	0.06			ktan	5.46	5.33
25	50.06	−0.59	71.7	1.4	31.9	3.5	0.87	0.08			ktan	5.46	5.33

Notes: Column (1) is the sequential number for sources indicated in Figure A.3; Columns (2) and (3) are the Galactic longitude and latitude respectively; Columns (4) and (5) list the centroid velocity and its 1σ uncertainty respectively; Columns (6) and (7) give the FWHM line width and its 1σ uncertainty respectively; Columns (8) and (9) are the integrated intensity and its uncertainty respectively; Column (10) gives the cross-identifications from SIMBAD, references: (a) Simpson et al. (2012); (b) Beichman et al. (1988); (c) Kang et al. (2009); (d) Spitzer Science (2009); Column (11) is the angular distance between the RRL source and possible association; Column (12) gives notes for: kfar − the farther kinematic distance is adopted, ktan − the source is located at the tangent point and the distance to the tangent is adopted; Column (13) lists the distance to the Sun which is calculated with a flat rotation curve with the IAU standard $R_0 = 8.5\,$kpc, $\Theta_0 = 220\,$km s^{-1} and the standard solar motions of $U_\odot = 10.27\,$km s^{-1}, $V_\odot = 15.32\,$km s^{-1} and $W_\odot = 7.74\,$km s^{-1}; Column (14) is the same as Column (13), except with $R_0 = 8.3\,$kpc, $\Theta_0 = 239\,$km s^{-1} (Reid et al. 2014) and the solar motions of $U_\odot = 11.10\,$km s^{-1}, $V_\odot = 12.24\,$km s^{-1} and $W_\odot = 7.25\,$km s^{-1} (Schönrich et al. 2010).

References

Alves, M. I. R., Calabretta, M., Davies, R. D., et al. 2015, MNRAS, 450, 2025

Alves, M. I. R., Davies, R. D., Dickinson, C., et al. 2010, MNRAS, 405, 1654

Anderson, L. D., Armentrout, W. P., Johnstone, B. M., et al. 2015, ApJS, 221, 26

Anderson, L. D., & Bania, T. M. 2009, ApJ, 690, 706

Anderson, L. D., Bania, T. M., Balser, D. S., et al. 2014, ApJS, 212, 1

Anderson, L. D., Bania, T. M., Balser, D. S., & Rood, R. T. 2011, ApJS, 194, 32

Araya, E., Hofner, P., Churchwell, E., & Kurtz, S. 2002, ApJS, 138, 63

Azcárate, I. N., Cersosimo, J. C., Wilkes, L. M., & Cordero, Y. A. 1997, Ap&SS, 253, 313

Balser, D. S. 2006, AJ, 132, 2326

Balser, D. S., Rood, R. T., Bania, T. M., & Anderson, L. D. 2011, ApJ, 738, 27

Bania, T. M., Anderson, L. D., & Balser, D. S. 2012, ApJ, 759, 96

Beichman, C. A., Neugebauer, G., Habing, H. J., Clegg, P. E., & Chester, T. J., eds. 1988, Infrared Astronomical Satellite (IRAS) Catalogs and Atlases, Explanatory Supplement, 1

Bihr, S., Beuther, H., Ott, J., et al. 2015, A&A, 580, A112
Blitz, L., Fich, M., & Stark, A. A. 1982, ApJS, 49, 183
Brunthaler, A., Reid, M. J., Menten, K. M., et al. 2011, Astronomische Nachrichten, 332, 461
Caswell, J. L., & Haynes, R. F. 1987, A&A, 171, 261
Cersosimo, J. C. 1990, ApJ, 349, 67
Cersosimo, J. C., Azcarate, I. N., Hart, L., & Colomb, F. R. 1989, A&A, 208, 239
Cersosimo, J. C., Mader, S., Figueroa, N. S., et al. 2009, ApJ, 699, 469
Churchwell, E., Mezger, P. G., & Huchtmeier, W. 1974, A&A, 32, 283
Dame, T. M., Hartmann, D., & Thaddeus, P. 2001, ApJ, 547, 792
Dempsey, J. T., Thomas, H. S., & Currie, M. J. 2013, ApJS, 209, 8
Downes, D., Wilson, T. L., Bieging, J., & Wink, J. 1980, A&AS, 40, 379
Du, Z. M., Zhou, J. J., Esimbek, J., Han, X. H., & Zhang, C. P. 2011, A&A, 532, A127
Ferrière, K., Gillard, W., & Jean, P. 2007, A&A, 467, 611
Fich, M., Dahl, G. P., & Treffers, R. R. 1990, AJ, 99, 622
Gordon, M. A., & Cato, T. 1972, ApJ, 176, 587
Gordon, M. A., & Sorochenko, R. L., eds. 2009, Astrophysics and Space Science Library, 282, Radio Recombination Lines
Han, X.-H., Zhou, J.-J., Esimbek, J., Wu, G., & Gao, M.-F. 2011, RAA (Research in Astronomy and Astrophysics), 11, 156
Hart, L., & Pedlar, A. 1976, MNRAS, 176, 547
Heiles, C., Reach, W. T., & Koo, B.-C. 1996, ApJ, 466, 191
Hou, L. G., & Han, J. L. 2014, A&A, 569, A125
Hou, L. G., & Han, J. L. 2015, MNRAS, 454, 626
Hou, L. G., Han, J. L., & Shi, W. B. 2009, A&A, 499, 473
Kalberla, P. M. W., Burton, W. B., Hartmann, D., et al. 2005, A&A, 440, 775
Kang, M., Bieging, J. H., Povich, M. S., & Lee, Y. 2009, ApJ, 706, 83
Lequeux, J. 2005, The Interstellar Medium (Berlin: Springer)
Li, J., Shen, Z.-Q., Wang, J., et al. 2016, ApJ, 824, 136
Liu, B., McIntyre, T., Terzian, Y., et al. 2013, AJ, 146, 80
Lockman, F. J. 1976, ApJ, 209, 429
Lockman, F. J. 1989, ApJS, 71, 469
Lockman, F. J., Pisano, D. J., & Howard, G. J. 1996, ApJ, 472, 173
McClure-Griffiths, N. M., Dickey, J. M., Gaensler, B. M., et al. 2005, ApJS, 158, 178
McGee, R. X., & Newton, L. M. 1981, MNRAS, 196, 889
Menzel, D. H. 1968, Nature, 218, 756
Mezger, P. G., & Hoglund, B. 1967, ApJ, 147, 490
Quireza, C., Rood, R. T., Balser, D. S., & Bania, T. M. 2006, ApJS, 165, 338
Reid, M. J., Menten, K. M., Zheng, X. W., et al. 2009, ApJ, 700, 137
Reid, M. J., Menten, K. M., Brunthaler, A., et al. 2014, ApJ, 783, 130
Reifenstein, E. C., Wilson, T. L., Burke, B. F., Mezger, P. G., & Altenhoff, W. J. 1970, A&A, 4, 357
Rigby, A. J., Moore, T. J. T., Plume, R., et al. 2016, MNRAS, 456, 2885
Roshi, D. A., & Anantharamaiah, K. R. 2000, ApJ, 535, 231
Roshi, D. A., & Anantharamaiah, K. R. 2001, Journal of Astrophysics and Astronomy, 22, 81
Russeil, D. 2003, A&A, 397, 133
Schönrich, R., Binney, J., & Dehnen, W. 2010, MNRAS, 403, 1829
Sewilo, M., Watson, C., Araya, E., et al. 2004, ApJS, 154, 553
Silverglate, P. R., & Terzian, Y. 1979, ApJS, 39, 157
Simpson, R. J., Povich, M. S., Kendrew, S., et al. 2012, MNRAS, 424, 2442
Smirnov, G. T., Sorochenko, R. L., & Pankonin, V. 1984, A&A, 135, 116
Spitzer Science, C. 2009, VizieR Online Data Catalog, 2293
Stil, J. M., Taylor, A. R., Dickey, J. M., et al. 2006, AJ, 132, 1158
Thompson, M., Beuther, H., Dickinson, C., et al. 2015, Advancing Astrophysics with the Square Kilometre Array (AASKA14), 126
Wang, J. Q., Yu, L. F., Zhao, R. B., et al. 2015, Acta Astronomica Sinica, 56, 63
Watson, C., Araya, E., Sewilo, M., et al. 2003, ApJ, 587, 714
Wenger, M., Ochsenbein, F., Egret, D., et al. 2000, A&AS, 143, 9
Wilson, T. L., Mezger, P. G., Gardner, F. F., & Milne, D. K. 1970, A&A, 6, 364
Wink, J. E., Wilson, T. L., & Bieging, J. H. 1983, A&A, 127, 211
Xu, W. F., Gao, X. Y., Han, J. L., & Liu, F. S. 2013, A&A, 559, A81